# A comprehensive DFT and SCAPS simulation study of the structural, electronic, elastic, optical, thermoelectric, and photovoltaic properties of the double perovskite $Cs_2PbSnBr_6$

M. Ghalab*, A. Arrar, and C. A. Hadj

*Laboratory of Physics Thin Layer & Advanced Technologies, Department of Physics, Faculty of Science and Technology, University of RELIZANE, Bourmadia, BP 48000, W. Relizane, Algeria,*
**e-mail: mohamed.ghaleb@univ-relizane.dz; Tel. +213799035690*

Received 5 September 2025; accepted 2 January 2026

This study presents a comprehensive investigation of the double perovskite $Cs_2PbSnBr_6$ using first-principles Density Functional Theory (DFT) calculations and SCAPS-1D device simulations to explore its structural, electronic, elastic, optical, thermoelectric, and photovoltaic properties. The structural analysis confirms the cubic phase (space group Fm-3m) with excellent mechanical stability, as evidenced by elastic constants and bulk modulus (18.88 GPa). Electronic band structure calculations, performed using TB-mBJ + SOC, reveal a direct bandgap of 1.63 eV. High optical responsiveness is observed in the material, possessing large absorption coefficients ($\sim 10^5$ cm$^{-1}$) in the visible and UV range and low reflectivity. Thermoelectric analysis indicates promising performance, with a high Seebeck coefficient and power factor ($\sim 10^{12}$ a.u.). SCAPS-1D simulations demonstrate outstanding photovoltaic performance, achieving a power conversion efficiency (PCE) of up to 31.8% under optimized conditions, with a high open-circuit voltage ($V_{oc} \sim 1.61$ V) and fill factor (FF $\sim 86.7\%$).

*Keywords:* Double perovskite; DFT; SCAPS-1D; $Cs_2PbSnBr_6$; photovoltaic properties; thermoelectric properties.

DOI: https://doi.org/10.31349/RevMexFis.72.031001

## 1. Introduction

In light of the numerous international conferences dedicated to addressing global environmental challenges and reducing atmospheric carbon dioxide emissions, there has been a growing shift in focus toward solar energy as a sustainable solution. Nevertheless, conventional solar cells have struggled to meet the escalating global energy demand, largely due to material scarcity and limited efficiency. Perovskite materials have emerged as a ray of hope in this field. Their remarkable properties including strong light absorption, high charge-carrier mobility, long diffusion lengths, and tunable bandgaps position them at the forefront of next-generation photovoltaic technologies. Among these materials, mixed cation/halide perovskites offer greater freedom in structural and electronic engineering, allowing precise control of photovoltaic behavior.

As always with this unique class of compounds continues to captivate researchers in the field of solar energy than much research has been conducted on perovskite solar cells (PSCs), where the power conversion efficiency (PCE) of these lead halide-based organic-inorganic hybrid cells has rapidly increased from 3.8% to a record-breaking certified efficiency of 30% [1, 2]. These cells hold remarkable promise due to the ease of device fabrication using simple and inexpensive manufacturing methods and the abundance of their materials. Their poor stability against heat, humidity, and UV radiation has been a major obstacle to date [3].

Lead-based perovskite solar cells have attracted significant attention for their combination of exceptional efficiency and relatively good stability compared to other perovskite compositions. Recent studies confirm that while challenges remain, lead halide perovskites have exhibited remarkable stability improvements that enable consideration for commercial applications. The certified power conversion efficiency (PCE) of single-junction lead halide PSCs has increased significantly, reaching approximately 26.7% in 2024 and over 32% in early 2025, approaching the performance of tandem silicon solar cells [4,5]. However, stability challenges remain due to intrinsic and extrinsic degradation mechanisms, but active research on material composition, additives, and device engineering has led to greatly improved operational stability and moisture resistance [6]. A recent approach used biomass-derived additives that interact with and immobilize lead ions in the perovskite structure, reducing defects and lead leakage while enhancing moisture resistance. Such devices achieved 25.01% PCE and retained over 95% of their performance after 2000 hours of storage and 80% efficiency under humid illumination for 1050 hours, showing promising commercial viability [7]. The lead perovskite systems focus on balancing high efficiency with controlled lead toxicity risks through chemical passivation strategies and physical encapsulation, crucial for market acceptance [8]. Lead halide perovskites feature a combination of exceptional efficiency and significantly enhanced stability compared to their peers, enhancing their potential for commercial solar cell applications [2, 4, 9].

Pb-Sn alloys suppress $Sn^{4+}$ formation via lattice strain homogenization, enabling stable black-phase perovskites with post-treatments like F-TBA for defect passivation. Recent reviews highlight inorganic $CsSnI_3$ and Pb-Sn systems reaching prolonged stability (958 hours at 90% efficiency

retention) through $SnO_2$ ETL formation and 2D capping layer [10–12]. Double perovskites, particularly Pb/Sn-based systems, offer enhanced structural stability over single perovskites due to their ordered $A_2B(B')X_6$ framework, mitigating phase transitions and $Sn^{2+}$ oxidation that degrade efficiency in Sn perovskites. Lead-reduced and lead-free perovskite solar cells address toxicity concerns by substituting Pb with Sn, Ge, Bi, Sb, or double perovskite variants like $Cs_2SnI_6$, achieving up to 15% PCE while prioritizing environmental safety. High-efficiency SCAPS-1D simulations optimize these devices, predicting 28% PCE for Sn-based structures through absorber thickness tuning and defect passivation [13, 14].

Combining ab initio calculations with solar cell device simulations significantly reduces computational time and experimental effort while providing results that closely approximate experimental observations. For this reason, such integrated theoretical-device approaches have been widely adopted by researchers for the efficient evaluation and optimization of photovoltaic materials [15, 16].

Building on advances in lead-reduced perovskites, this work explores $Cs_2PbSnBr_6$, a double perovskite engineered by partially replacing lead with tin to combine high optical absorption with reduced toxicity. Leveraging state-of-the-art density functional theory (DFT) and advanced SCAPS simulations, we provide a comprehensive evaluation of its structural, electronic, and photovoltaic properties, positioning it as a promising candidate for next-generation high-efficiency solar cells.

## 2. Computational study and numerical simulations

In this study, we perform a combined theoretical and simulation-based investigation by integrating Density Functional Theory (DFT) calculations with solar cell modeling using the well-established SCAPS-1D software.

### 2.1. First-principles calculations of the $Cs_2PbSnBr_6$ absorber using density functional theory

In this work, Density Functional Theory (DFT) was employed as the foundational framework for the theoretical analysis, with the Kohn-Sham equations [17] solved using the full-potential linearized augmented plane wave (FP-LAPW) method implemented in the WIEN2k computational code [18]. This method is known for its high accuracy in treating the structural properties of complex materials. But as a first step, we carried out a precise optimization of the atomic positions of barium by accounting for variations in ionic radii, enabling sub-angstrom accuracy in atomic localization, with convergence up to $10^{-9}$ Å. This fine-tuning was essential to establish a reliable structural foundation for subsequent electronic and optical property calculations.

The structural properties were then investigated using the Generalized Gradient Approximation (GGA) with the Perdew-Burke-Ernzerhof (PBE) exchange-correlation functional. The robustness and reliability of the GGA-PBE framework have been confirmed through extensive benchmarking against experimental data in prior studies, making it an appropriate choice for the structural analysis conducted in this study [19–21].

However, it is well known that the standard Generalized Gradient Approximation with the Perdew-Burke-Ernzerhof (GGA-PBE) functional tends to systematically underestimate band gaps, particularly in materials with complex electronic interactions or significant relativistic effects. To address this limitation and achieve a more accurate estimation of the band gap and associated electronic properties close to experimental results, we employed the Tran-Blaha modified Becke-Johnson (TB-mBJ) exchange potential. This semi-local potential has demonstrated substantial improvement in band gap predictions across a wide range of semiconductors. A comparative study presented in Ref. [22] further supports the superiority of TB-mBJ over conventional approximations in this context. Additionally, to account for relativistic effects especially relevant for materials containing heavy atoms, we incorporated spin-orbit coupling (SOC) into our calculations. The combined application of TB-mBJ and SOC provides a more accurate and physically realistic representation of the electronic structure and last properties.

For our computational setup, the muffin-tin radius (RMT) for each of the four atomic species was uniformly set at 2.35 Bohr. The key input parameters Rkmax, Gmax, and Kpoint were carefully chosen as 8, 12, and 1000, respectively. These selections correspond to a basis set comprising 256 plane waves and a $(10 \times 10 \times 10)$ k-point mesh within the First Brillouin Zone. Additionally, a threshold energy of $-6.0$ Ryd was employed to effectively distinguish between core and valence electronic states in the calculations.

### 2.2. SCAPS-1D numerical simulation of $Cs_2PbSnBr_6$

In this study, a planar n-p perovskite solar cell architecture was employed, comprising fluorine-doped tin oxide (FTO), an electron transport layer (ETL), a perovskite absorber, and a hole transport layer (HTL), as illustrated in Fig. 6. The simulation was conducted under standard test conditions: a temperature of 300 K, an illumination intensity of 1000 W/m$^2$ corresponding to the AM1.5G solar spectrum, an electron-hole thermal velocity of $10^7$ cm/s, and a uniform defect density of $10^{15}$ cm$^{-3}$. All simulations were carried out using the widely used SCAPS-1D software [23]. A detailed summary of the simulation parameters is provided in Table III.

The input parameters were carefully determined based on first-principles (DFT) calculations. Specifically, the effective masses were extracted from the electronic band structure

$$m^* = \left( \frac{\hbar}{\frac{\partial^2 E}{\partial k^2}} \right),$$

while the dielectric constant ($\epsilon_F$) was obtained from the real and imaginary parts of the calculated optical dielectric func-

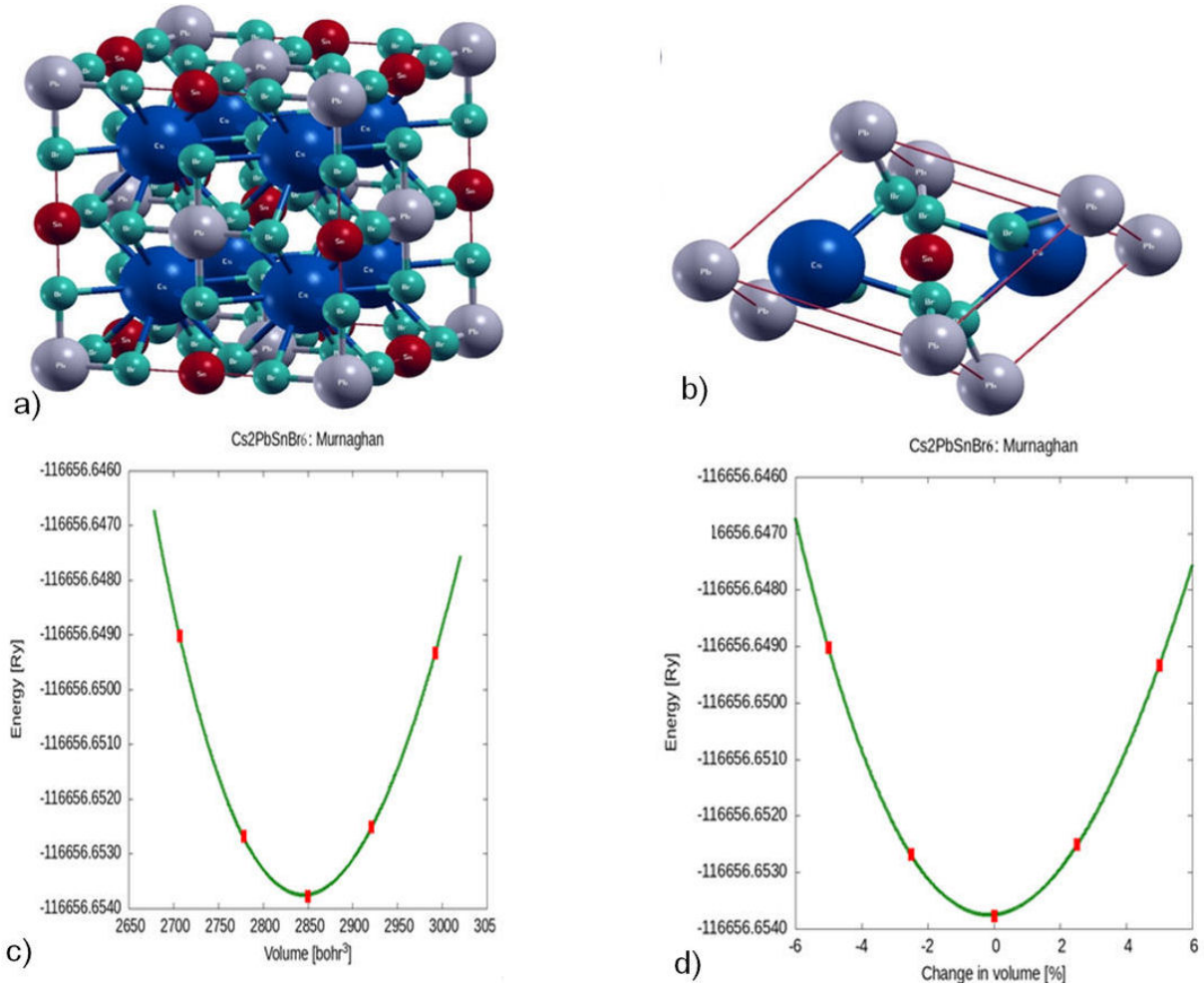


FIGURE 1. The cubic crystal structure for the $Cs_2PbSnBr_6$ double perovskite: a) conventional cell, b) primitive cell, c) total energy (Ry) vs unit cell volume (bohr$^3$) for the $Cs_2PbSnBr_6$ double perovskite.

tion. The electron affinity ($\chi$(eV)) was evaluated through a total energy difference approach by introducing an additional electron into the system. The remaining parameters were derived consistently using effective mass approximations.

## 3. Results and discussion

### 3.1. Wien2K simulation

#### *3.1.1. Structural properties*

In the initial phase of our investigation, we focus on the structural properties of $Cs_2PbSnBr_6$, employing the approximation (GGA-PBE) framework. Subsequent analyses of the electronic, optical, elastic, and thermodynamic properties are carried out using the Tran-Blaha modified Becke-Johnson potential (TB-mBJ) with spin-orbit coupling (SOC) included, ensuring a more accurate description of the band structure. The study is conducted in the cubic phase of the compound, corresponding to the space group Fm-3m (No. 225). To determine the equilibrium structural parameters, we apply the Murnaghan equation of state, generating an Energy-Volume ($E-V$) curve. This allows us to extract key physical quantities such as the equilibrium volume, lattice constant, bulk modulus, and pressure derivative. The resulting $E-V$ relationship and the associated structural parameters are illustrated in Fig. 1c).

In the cubic $A_2BB'X_6$ double perovskite structure, the divalent metal cations $B^{2+}$ and $B'^{2+}$ are each octahedrally coordinated by six halide anions ($X^-$), forming $BX_6$ and $B'X_6$ octahedra. These octahedra are interconnected via corner-sharing, where each halide ion bridges two adjacent metal centers. In an ideal cubic configuration, the B-X and B′-X bonds are linearly aligned, resulting in a B-X-B′ bond angle of 180°, which reflects the high symmetry and uniformity of the structure. Concerning the atomic arrangement in the unit cell, the A-site cations are positioned at the centers of the cubes, the B' cations occupy the cube corners (vertices), and the B cations are located at the midpoints of the cube edges. This geometrical configuration corresponds to the highly symmetric space group Fm-3m (No. 225). The Brillouin zone of the cubic lattice includes high-symmetry points such as Γ at (0, 0, 0), L at (1/2, 1/2, 1/2), and W, which lies at (1/2, 1, 0) in reciprocal space.

TABLE I. Lattice parameters (Å), bulk modulus (GPa), derivative B', minimum total energy (Ry), and GAP (eV) using PBE-GGA.

| Compound | $a$ (Å) | $V$ (a.u.$^3$) | $B$ (GPa) | $B'$ | $E_{tot}$ (Ry) | $GAP_{GGA\text{-}PBE}$ (eV) | Ref. |
|---|---|---|---|---|---|---|---|
| $Cs_2PbSnBr_6$ | 11.9030 | 2845.1328 | 18.8788 | 4.6959 | -116656.653753 | 1.2 | This work |
| $Cs_2ScInI_6$ | 12.15 | 2074.7500 | 17.95 | | | 0.95 | [25] |
| $Rb_2ScInI_6$ | 12.12 | 2449.7600 | 18.85 | | | 0.90 | [25] |
| $Cs_2CaGeI_6$ | 12.26 | 3112.7900 | 16.1551 | 4.6037 | -122149.836581 | 2.82 | [26] |
| $Cs_2ZnPbBr_6$ | 11.3451 | 2463.5850 | 22.9608 | 4.8664 | -107890.582888 | 1.727 | [27] |
| $Cs_2ZnPbCl_6$ | 10.7643 | 2104.2488 | 27.8476 | 4.7126 | -82148.981671 | 2.472 | [27] |

The cubic unit cell contains a single formula unit of the compound, with atomic positions defined by specific Wyckoff sites: Cs occupies the 8c position at (0.25, 0.25, 0.25), Pb is located at 4a (0, 0, 0), Sn at 4b (0.5, 0.5, 0.5), and Br atoms are distributed over the 24e sites with fractional coordinates (0.25230039, 0, 0) Figs. 1a), 1b). This well-defined crystallographic configuration provides the foundation for analyzing the compound's structural stability and its subsequent electronic and optical behavior.

To determine the ground-state properties of the $Cs_2PbSnBr_6$ compound, we performed self-consistent calculations by solving the Kohn-Sham equations within the framework of density functional theory. These calculations allowed us to evaluate the total energy as a function of the unit cell volume. The corresponding results are presented in Table I. The optimized structural parameters, including the lattice constant $a$, bulk modulus $B$, and its pressure derivative $B'$, were extracted and are listed in Table I. These values are compared with theoretical data from other calculations to assess the reliability of our computational approach, as shown in Table I. The energy-volume data obtained from structural optimization were fitted using the Birch-Murnaghan equation of state [24], and the resulting $E - V$ curve is illustrated in Fig. 2. The Murnaghan equation is expressed as follows:

$$E(V) = E_0 + \left(\frac{9V_0B_0}{16}\right)\left\{\left[\left(\frac{V_0}{V}\right)^{\frac{2}{3}} - 1\right]^3 B_0' + \left[\left(\frac{V_0}{V}\right)^{\frac{2}{3}} - 1\right]^2 \left[6 - 4\left(\frac{V_0}{V}\right)^{\frac{2}{3}}\right]\right\}. \quad (1)$$

Table I shows that a higher bulk modulus $B$ indicates greater compressive strength. This increase in compressive strength correlates directly with enhanced material hardness, signifying improved resistance to mechanical deformation such as indentation, scratching, or penetration [28]. Figure 2 shows a 2D slice with atom labels and colored contours representing the electron distribution in the unit cell. The figure displays a 2D contour plot of the charge density, projected onto a specific crystallographic plane intersecting Cs, Pb, Sn, and Br atoms.

The charge density is represented by a color gradient, where red regions indicate high electron density and blue regions correspond to low electron density. As observed, there is a significant electron accumulation around the halide (Br) atoms, indicating their high electronegativity and strong tendency to attract charge from neighboring metal cations. The Pb-Br and Sn-Br bonds exhibit moderate electron sharing, consistent with a mixed ionic-covalent bonding character, which is typical of halide perovskites.

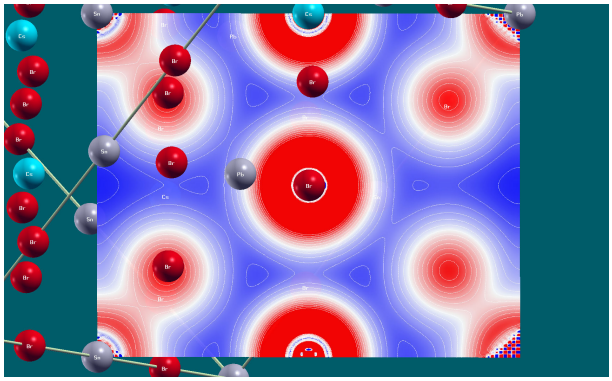

FIGURE 2. Electron density map of the double perovskite $Cs_2PbSnBr_6$.

Moreover, there is a vertical overlap between the cesium and barium atoms, and as can be seen in Fig. 1, there is a bond between the cesium atoms and the rest of the atoms which cesium plays a structural role as a charge-balancing monovalent cation. The charge localization near Sn and Pb centers suggests different extents of hybridization with Br-p orbitals, which may influence the electronic band structure and carrier effective masses, parameters critical for photovoltaic performance.

This charge density confirms the structural stability of the optimized $Cs_2PbSnBr_6$ lattice but also supports the presence of semiconducting behavior.

### 3.1.2. *Electronic properties*

The electronic properties play a critical role in defining the functional behaviour of this material, particularly in photovoltaic applications. These properties govern light absorption across various wavelengths and the subsequent generation of electron-hole pairs, processes fundamental to solar cell performance. Given their importance, it is essential to ensure a high degree of accuracy in the calculation of electronic char-

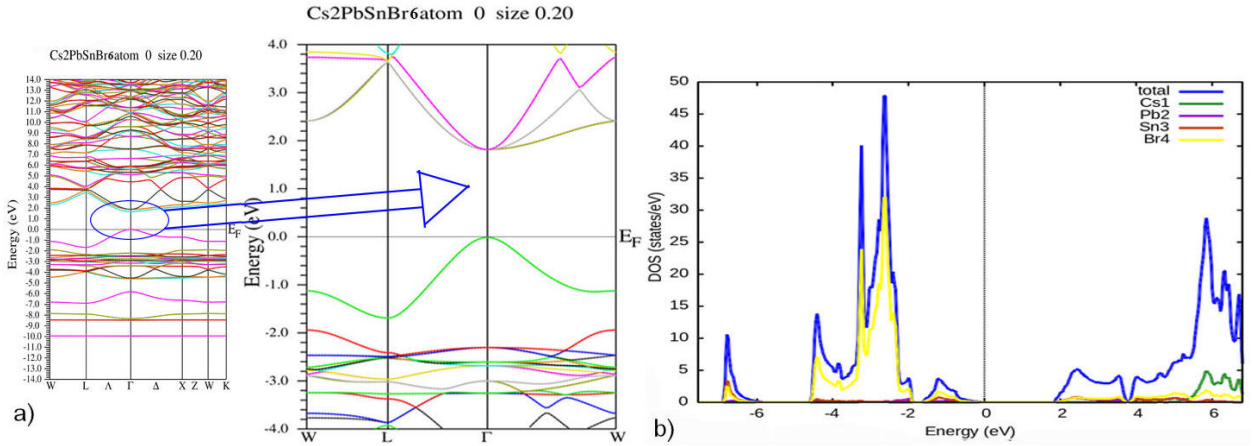


FIGURE 3. a) Electronic band structure and b) total and partial density of states (TDOS and PDOS) of the $Cs_2PbSnBr_6$ compound calculated using the TB-mBJ potential with spin-orbit coupling (SOC).

acteristics. As previously noted, we employ the (TB-mBJ) in combination with (SOC) to achieve a more precise estimation of the band gap, in closer agreement with experimental results.

As illustrated in Fig. 3, the compound exhibits a direct band gap of 1.63 eV, with the valence band maximum located near the Fermi level. This proximity facilitates efficient electron transfer at material interfaces, enhances carrier generation, and lowers the energy threshold required for electron excitation, key factors for improving photovoltaic performance [19,29]. The conduction band of $Cs_2PbSnBr_6$ is composed of three distinct sub-bands, each exhibiting a unique curvature that corresponds to a different effective mass for the charge carriers Fig. 3a). These variations in curvature lead to differences in electron mobility across the sub-bands, directly influencing the speed and efficiency of charge transport within the material [30]. Such band structure characteristics are particularly advantageous for photovoltaic and photodetector applications, as they promote rapid charge separation and facilitate efficient carrier collection. Furthermore, the presence of multiple conduction sub-bands enables the material to interact with a broader range of photon energies [31].

Electrons can be excited into different energy levels within the conduction band depending on the incident photon energy, thereby improving light absorption and contributing to enhanced utilization of the solar spectrum. This complexity in the electronic structure supports higher overall device efficiency and underscores the material's potential for high-performance optoelectronic applications.

The density of states (DOS) illustrated in Fig. 3b) reinforces the band structure analysis, showing that the valence band maximum is dominated by Br-p states, with hybridized contributions from Pb-p and Sn-p orbitals, consistent with the electronic structure of halide double perovskites. Meanwhile, the conduction band features a more intricate hybridization of atomic orbitals, reflecting the complex electronic interactions within the crystal structure.

### *3.1.3. Optical properties*

The optical characteristics of a material are critical in determining its suitability for optoelectronic applications. To gain a better understanding of the interaction between the material and electromagnetic radiation, we computed its optical properties using the Tran-Blaha modified Becke-Johnson (TB-mBJ) exchange potential. Figure 4 presents the important optical response functions, including the complex dielectric function $\epsilon_F(\omega) = \epsilon_1(\omega) + i\epsilon_2(\omega)$, absorption coefficient $\alpha(\omega)$, refractive index $n(\omega)$, optical loss function $L(\omega)$, and reflectivity $R(\omega)$. **Complex Dielectric Function $\epsilon_F$:** The complex dielectric function, $\epsilon_F(\omega) = \epsilon_1(\omega)+i\epsilon_2(\omega)$, characterizes the frequency-dependent response of a material's electrons to incident electromagnetic radiation for $Cs_2PbSnBr_6$, the real part $\epsilon_1(\omega)$ is associated with the material's polarization response and is inversely related to the band gap energy $E_g$, consistent with the Penn model [32]. The imaginary part $\epsilon_2(\omega)$, on the other hand, describes the absorption behavior of the material and quantifies how strongly it interacts with electromagnetic waves at various photon energies. As shown in the spectral profile [Fig. 4a)], both the real and imaginary components of the dielectric function begin to rise at approximately 1.5 eV (corresponding to a wavelength of $\sim 826$ nm), reaching their respective maxima around 3.0 eV ($\sim 413$ nm). Beyond this peak, a gradual decline is observed, followed by oscillatory behavior in the ultraviolet region. This spectral evolution indicates that the $Cs_2PbSnBr_6$ compound exhibits strong optical activity within the visible range, suggesting its high potential for optoelectronic applications, particularly in photovoltaic and photodetection devices.

**Absorption Coefficient $\alpha$:** The excitation of an electron from the valence band, across the band gap, to the conduction band and into unoccupied (empty) states requires the absorption of photons with sufficient energy. The absorption coefficient, $\alpha(\omega)$, is a critical parameter that quantifies the amount of optical power absorbed per unit length as electromagnetic radiation propagates through a material.

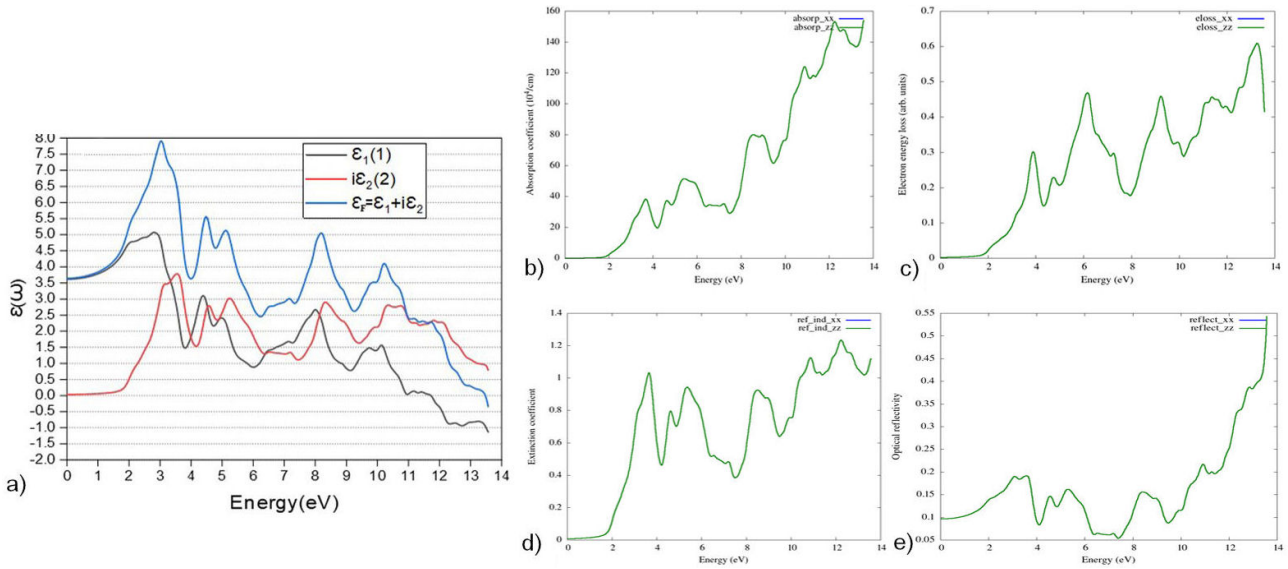


FIGURE 4. a) Dielectric functions, b) Absorption coefficient, c) Loss factor, d) Refractive index, and e) Reflectivity for $Cs_2PbSnBr_6$.

The absorption spectrum of $Cs_2PbSnBr_6$, presented in Fig. 4b), reveals anisotropic optical behavior across the examined energy range. The absorption onset begins around 1.6 eV (corresponding to a wavelength of $\sim 774$ nm), which corresponds to the band gap, indicating the material's initial interaction with incident photons in the near-infrared region. A pronounced absorption peak is observed at approximately 3.5 eV ($\sim 345$ nm), marking the first major optical transition. Additional absorption edges are visible at 5 and 9 eV, followed by a series of distinct successive peaks extending up to 14 eV, indicating strong and complex optical transitions in the ultraviolet (UV) range. This high absorbance in the UV region suggests that $Cs_2PbSnBr_6$ is an auspicious material for ultraviolet photodetection and sensing applications.

**The optical loss function,** $L(\omega)$, characterizes the energy loss of fast electrons traversing a material and provides insights into plasmonic and interband transition behavior. As shown in Fig. 4c), the optical energy loss for $Cs_2PbSnBr_6$ remains relatively low throughout the visible spectrum, not exceeding a value of 0.3. This indicates minimal energy dissipation and high optical efficiency within the visible range. However, in the ultraviolet region, the loss function reaches a peak of approximately 0.6. This trend suggests that while the material maintains low-loss behavior in the visible range, beneficial for optoelectronic performance, it exhibits more pronounced energy loss in the ultraviolet, consistent with strong electronic excitations.

The variation of **the refractive index**, $n(\omega)$, as a function of photon energy for $Cs_2PbSnBr_6$ is presented in Fig. 4d). Its value in the visible ranges from 0.48 at 300 nm to 0.02 at 900 nm, with a resonance peak at 326 nm and a maximum value of 1.2, indicating strong dispersion behavior typical of semiconducting materials. In the ultraviolet (UV) region, $n(\omega)$ exhibits oscillatory behavior with alternating increases and decreases, reaching its highest value near 100 nm. These characteristics reflect the material's strong interaction with high-energy photons.

**Reflectivity** $R(\omega)$**:** The reflectivity spectrum of $Cs_2PbSnBr_6$, shown in Fig. 4e), reveals a relatively low reflectance, not exceeding 0.45% from 0 to 12 eV. This low reflectivity is characteristic of semiconducting materials with strong photon absorption and minimal surface reflection. The combination of a high absorption coefficient, promising electronic conductivity, and low reflection confirms the potential of $Cs_2PbSnBr_6$ for energy-related applications, particularly in photovoltaic and photodetector devices, where efficient light harvesting and minimal optical losses are critical.

The analysis of the optical properties of $Cs_2PbSnBr_6$ reveals enhanced performance in comparison with certain other perovskite materials, particularly in terms of strong UV absorption, low reflectivity, and favorable dielectric behavior. These characteristics suggest that the compound holds promise for optoelectronic and energy-related applications. In the following study, we will further investigate its potential suitability for solar cell integration through detailed electronic and device-level simulations.

### *3.1.4. Elastic properties*

Elastic constants are essential for evaluating a material's mechanical behavior and its ability to resist deformation under external stress. Specifically, the second-order elastic constants $C_{11}$, $C_{12}$, and $C_{44}$ provide valuable insights into the structural stability, interatomic bonding strength, and anisotropic mechanical response of the material. For cubic crystals, these three independent constants are sufficient to fully characterize the elastic response.

In this study, the IRLASE package integrated with the WIEN2k code was employed to calculate the elastic constants of $Cs_2PbSnBr_6$. The computed values of $C_{11}$, $C_{12}$, and $C_{44}$ are listed in Table II. According to the Born stability

TABLE II. Elastic parameters for $Cs_2PbSnBr_6$.

| Parameter | $Cs_2PbSnBr_6$ |
|---|---|
| $C_{11}$ - $C_{12}$ (GPa) | 83.742 |
| $C_{11}$ + 2$C_{12}$ (GPa) | 100.199 |
| $C_{44}$ (GPa) | 10.527 |
| Voigt Bulk Modulus (GPa) | 33.399 |
| Reuss Bulk Modulus (GPa) | 33.399 |
| Voigt Shear Modulus (GPa) | 23.065 |
| Reuss Shear Modulus (GPa) | 15.026 |
| Hill Shear Modulus (GPa) | 19.046 |
| Voigt Young Modulus (GPa) | 56.246 |
| Reuss Young Modulus (GPa) | 39.200 |
| Hill Young Modulus (GPa) | 48.011 |
| Voigt Poisson's Coefficient | 0.219 |
| Reuss Poisson's Coefficient | 0.304 |
| Hill Poisson's Coefficient | 0.260 |
| Transverse Elastic Wave Velocity (m/s) | 1949.242 |
| Longitudinal Elastic Wave Velocity (m/s) | 3424.778 |
| Debye Temperature (K) | 196.304 |

criteria for cubic systems [33], $C_{11} > 0$, $C_{11} + 2C_{12} > 0$, and $C_{11} - C_{12} > 0$, the compound satisfies all conditions, confirming its mechanical stability.

Additionally, various macroscopic elastic moduli, including the bulk modulus, shear modulus, and Young's modulus, were derived using standard elasticity relations as detailed in Ref. [34]. These parameters further contribute to understanding the mechanical resilience and potential applicability of $Cs_2PbSnBr_6$ in structural and optoelectronic devices.

### *3.1.5. Thermoelectric properties*

In this section, we investigate the thermoelectric properties of the double perovskite $Cs_2PbSnBr_6$ using the BoltzTraP module interfaced with the WIEN2k package. The calculations are performed within the framework of the semi-classical Boltzmann transport theory under the constant relaxation time approximation [35]. In this approach, the BoltzTraP code applies the finite-temperature thermal smearing of the Fermi-Dirac distribution to the DFT-derived electronic band structures to evaluate the thermoelectric transport coefficients [36]. All transport quantities are obtained from energy integrals of the form:

$$\int \sum(E) \left( -\frac{\partial f(E,T)}{\partial E} \right), \tag{2}$$

where $\Sigma(E)$ represents the transport distribution function [37].

The key thermoelectric parameters-including the electrical conductivity normalized by the relaxation time ($\sigma/\tau$), the Seebeck coefficient $S$, and the power factor (PF) are calculated as functions of both chemical potential and temperature. The resulting trends, which provide insight into the thermoelectric performance and energy-conversion potential of $Cs_2PbSnBr_6$, are presented in Fig. 5.

Figure 5a) shows the variation of the electrical conductivity scaled by the relaxation time ($\sigma/\tau$) of $Cs_2PbSnBr_6$ as a function of chemical potential ($\mu - \epsilon_F$) at different temperatures (300 K, 350 K, 500 K, and 600 K). The results reveal that the electrical conductivity exhibits multiple peaks as the chemical potential shifts across the energy, as increasing density of states in both the valence and conduction bands play a role in that. In particular, the double perovskite $Cs_2PbSnBr_6$, the relatively steep edge of the valence band plays a crucial role in enhancing conductivity, as the density of states rises rapidly just below the valence band maximum. This steep gradient in the density of states near the Fermi level leads to a high concentration of thermally excited charge carriers, thereby promoting electrical conductivity [38]. Furthermore, in the conduction band region between 1.7 and 6 eV, TDOS increases markedly, with dominant contributions from Pb-p and Sn-p orbitals and additional hybridization with Br-p states (Fig. 3). This increase in TDOS accounts for the pronounced peak in electrical conductivity scaled by the relaxation time ($\sigma/\tau$) observed at approximately 2 eV, as shown in [Fig. 5a)].

Furthermore, the involvement of multiple conduction bands with different band curvatures (Fig. 3-a) enhances carrier velocities by providing transport channels with varying effective masses, which further contributes to the overall increase in electrical conductivity [39]. As the temperature increases, the $\sigma/\tau$ curves broaden slightly but maintain the same overall profile, suggesting that the electrical conductivity in $Cs_2PbSnBr_6$ is moderately temperature-dependent within this range, and the ability of perovskites to withstand high temperatures is also noteworthy.

Figure 5b) illustrates the variation of the Seebeck coefficient $S$ (V/K) as a function of chemical potential ($\mu - \epsilon_F$) with the different temperatures, for the double perovskite $Cs_2PbSnBr_6$. The Seebeck coefficient exhibits a pronounced peak centered near the Fermi level ($\mu - \epsilon_F \approx 0$ eV), reaching a maximum value of approximately (0.0016 V/K). The curve demonstrates clear symmetric behavior concerning the Fermi level, which is characteristic of semiconductors. As the temperature increases, the magnitude of the peak slightly diminishes, which can be attributed to enhanced carrier diffusion and thermal broadening, a typical effect of increased lattice vibrations and carrier scattering at elevated temperatures. This behavior is indicative of p-type transport, where hole conduction dominates. For higher chemical potentials, especially those deep in the conduction band.

Figure 5c) shows the Power Factor vs Chemical Potential at different temperatures ($T$ = 300 K, 350 K, 500 K, 600 K). The power factor exhibits a highly asymmetric behavior around the Fermi level; multiple sharp peaks in the power factor are observed, suggesting resonant energy levels or DOS features that enhance carrier transport. With increasing temperature, the peaks broaden and slightly decrease in

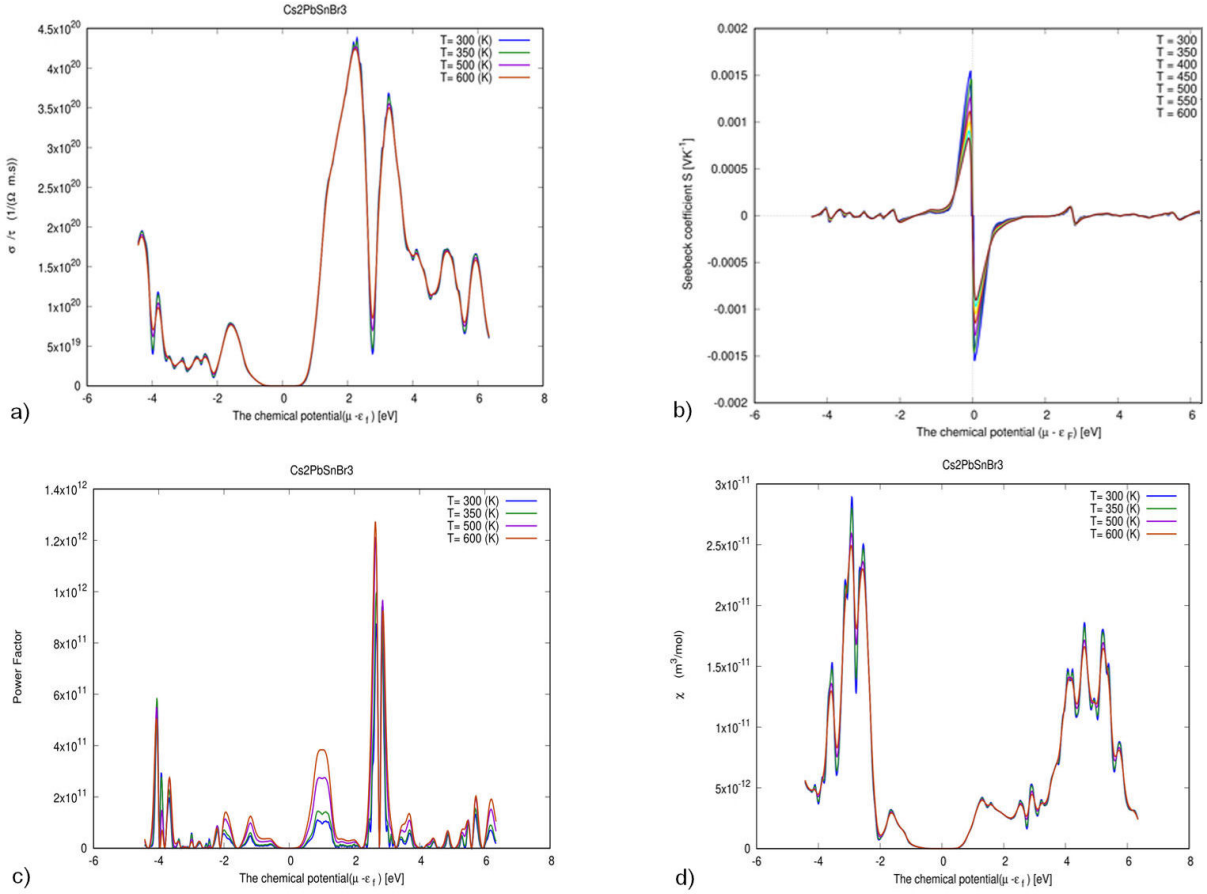


FIGURE 5. Thermoelectric Transport Properties of $Cs_2PbSnBr_6$: a) Electrical conductivity, b) Seebeck coefficient, c) Power factor and d) Magnetic susceptibility, as a function of chemical potential for different temperatures.

amplitude. At 300 K, the peaks are sharper and higher; at 600 K, they are slightly flatter. This broadening is typical due to thermal smearing of the Fermi-Dirac distribution, which reduces the sharpness of carrier distribution near the energy bands [40]. The PF in the order of $10^{12}$ (a.u.) indicates this material can achieve high thermoelectric performance, especially under optimized p-type conditions.

Figure 5d) depicts the variation of the magnetic susceptibility $\chi$ ($m^3$/mol) as a function of chemical potential for $Cs_2PbSnBr_6$ at different temperatures. The graph reveals several peaks and valleys in susceptibility, indicating a strong dependence on the electronic structure near the Fermi level. The most significant peaks occur in the region around $\mu - \epsilon_F \approx -2$ to $-4$ eV, where $\chi$ reaches values close to $3 \times 10^{-11}$ $m^3$/mol. These peaks correspond to high DOS near the valence band and suggest enhanced paramagnetic response due to increased carrier availability in those energy regions. The overall susceptibility curve remains relatively stable across the temperature range, indicating that electronic structure rather than thermal effects primarily governs magnetic response in this material. This behavior points to a diamagnetic to weakly paramagnetic nature of $Cs_2PbSnBr_6$, with the peaks in susceptibility associated with localized electronic states or band edge effects.

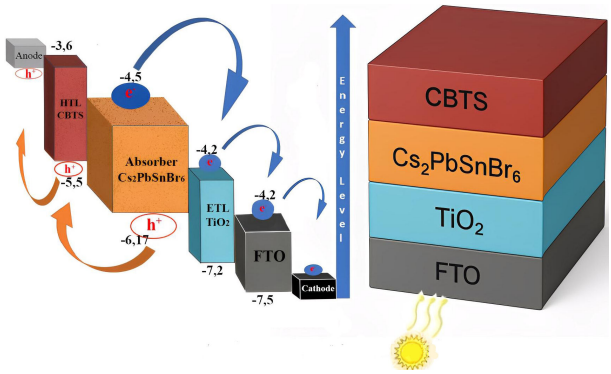


FIGURE 6. Schematic diagram of FTO/ETL/Perovskite/HTL heterojunction solar cell.

### 3.2. Solar cell simulation

After completing the DFT calculations, we proceed to evaluate the device-level photovoltaic performance of the double perovskite compound $Cs_2PbSnBr_6$ using the SCAPS-1D simulation software. As depicted in the Schematic Diagram (Fig. 6), the heterojunction architecture consists of a transparent conductive oxide (FTO) layer, an electron transport layer ($TiO_2$), the perovskite absorber we study, and a hole

TABLE III. Physical parameters employed in our solar cell simulations.

| Parameter | HTL (CBTS) | $Cs_2PbSnBr_6$ | ETL ($TiO_2$) | FTO |
|---|---|---|---|---|
| Layer thickness ($\mu$m) | 0.1 | Varied | 0.05 | 0.3 |
| Dielectric constant ($\epsilon$) | 5.4 | 3.65 | 9.00 | 3.50 |
| Band gap $E_g$ (eV) | 1.9 | 1.65 | 3.20 | 4.00 |
| Electron affinity $\chi$ (eV) | 3.6 | 4.54 | 4.10 | 9.00 |
| Effective conduction band density $N_c$ ($cm^{-3}$) | $2.2 \times 10^{18}$ | $2.44 \times 10^{17}$ | $2.0 \times 10^{18}$ | $2.20 \times 10^{18}$ |
| Effective valence band density $N_v$ ($cm^{-3}$) | $1.8 \times 10^{19}$ | $3.71 \times 10^{16}$ | $1.8 \times 10^{19}$ | $1.80 \times 10^{19}$ |
| Electron mobility $\mu_e$ ($cm^2\ V^{-1}\ s^{-1}$) | 30 | 1351 | 20 | 20 |
| Hole mobility $\mu_h$ ($cm^2\ V^{-1}\ s^{-1}$) | 10 | 132.8 | 10 | 10 |
| Shallow uniform donor density $N_d$ ($cm^{-3}$) | – | 0 | $9.0 \times 10^{16}$ | $1.00 \times 10^{21}$ |
| Shallow uniform acceptor density $N_a$ ($cm^{-3}$) | $1.0 \times 10^{18}$ | $1.2 \times 10^{16}$ | – | – |
| Defect density $N_t$ ($cm^{-3}$) | $1 \times 10^{15}$ | Varied | $1 \times 10^{15}$ | $1 \times 10^{15}$ |
| Reference | [41] | Calculated | [42] | [43] |

transport layer (CBTS), forming the complete device stack. This part aims to bridge the gap between fundamental material properties and practical solar cell design by assessing how effectively $Cs_2PbSnBr_6$ can function as an absorber layer in a complete photovoltaic device. To achieve this, we extract and calculate the necessary parameters for the simulation, as shown in Table III.

### *3.2.1. Effect of absorber layer thickness*

Figure 7a) illustrates the simulated variation of the open-circuit voltage ($V_{oc}$), density of current ($J_{sc}$), fill factor (FF), and power conversion efficiency (PCE) as a function of the $Cs_2PbSnBr_6$ absorber layer thickness, using the SCAPS-1D.

From the curves, it is evident that increasing the absorber layer thickness from 0.1 $\mu$m to 1.0 $\mu$m leads to significant performance improvements, particularly in $J_{sc}$ and PCE. This trend can be attributed to the enhanced light absorption and carrier generation with thicker layers. As the thickness increases, more photons are absorbed, leading to a higher number of electron-hole pairs, which directly contributes to the increase in $J_{sc}$ from PCE = 13.7% to 31.8% and $J_{sc} = 11.6$ mA/cm$^2$ to 22.6 mA/cm$^2$.

The $V_{oc}$ shows a slight increase with thickness going from 1.57 to 1.61 V. This subtle variation indicates that the built-in electric field and recombination mechanisms are relatively stable with thickness. The fill factor (FF) also improves rapidly in the thin-film regime (0.1 - 0.3 $\mu$m) before saturating at 86.7%, indicating enhanced charge extraction efficiency and lower series resistance with increasing thickness.

Considering the four variables, the ideal thickness of $Cs_2PbSnBr_6$ lies at 0.7 $\mu$m. This result highlights the strong potential of $Cs_2PbSnBr_6$ as an efficient lead-reduced absorber in thin-film photovoltaic cells. Figure 7b) displays the current-voltage (J-V) characteristic under standard illumination conditions (AM1.5G, 1000 W/m$^2$) for the heterojunction solar cell.

The J-V response shows a typical diode-like behavior with a steep increase in current as the voltage exceeds the built-in potential. The high $V_{oc}$: The x-intercept suggests a high open-circuit voltage, consistent with earlier analysis, which reported values around 1.61 - 1.62 V, indicative of low recombination and favorable band alignment.

Then the high $J_{sc}$ vertical intercept implies a strong photogenerated current, suggesting efficient light absorption and carrier collection, in line with the predicted $> 22$ mA/cm$^2$ from the previous simulation. The combination of high $V_{oc}$, $J_{sc}$, and sharp forward-bias behavior confirms the material's promise for high-efficiency lead-reduced perovskite solar cells. This performance is indicative of favorable interfacial energetics, optimized absorber thickness, and effective charge carrier dynamics.

The quantum efficiency (QE) spectrum of the heterojunction device in Fig. 7c). Quantum Efficiency (QE) shows the percentage of incident photons at a given energy that are converted into charge carriers (electrons or holes) collected by the electrodes [44]. We observe that the quantum efficiency in the infrared is low, almost zero, followed by a sharp increase up to 100% in the visible spectrum, and then by a gradual decrease in high-energy photons (UV). The sharp rise confirms the direct bandgap nature and highly efficient absorption, as well as efficient charge separation, implying good heterojunction band alignment between $TiO_2$, $Cs_2PbSnBr_6$, and CBTS.

### *3.2.2. Impact of defects in $Cs_2PbSnBr_6$ and interfaces on the device*

We will study the effect of the double perovskite defect and the defect of each of the two interfaces, $TiO_2/Cs_2PbSnBr_6$ and $Cs_2PbSnBr_6$/CBTS.

Looking at Fig. 8a), we observe that the effect of defect density on the photovoltaic parameters of the heterojunction cells indicates that the device maintains excellent perfor-

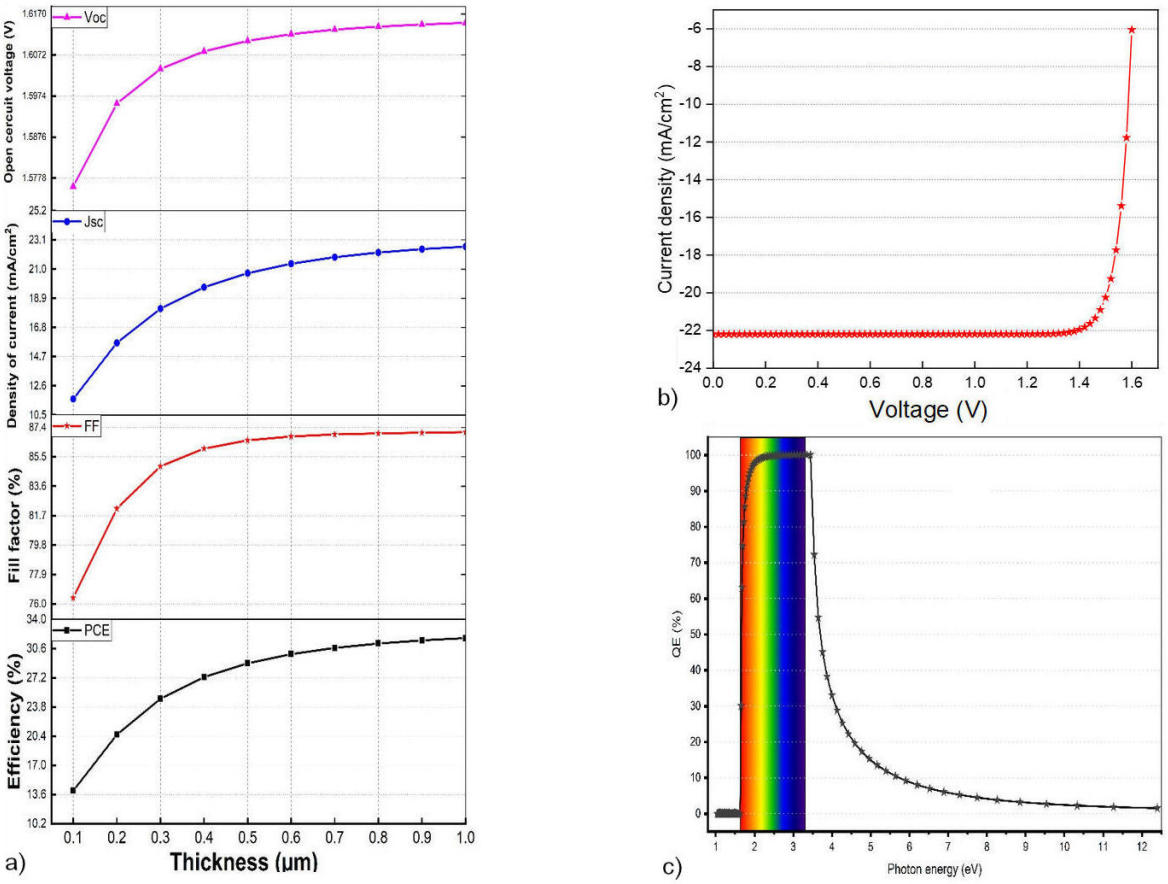


FIGURE 7. a) Optimization of the absorber layer thickness of the double perovskite $Cs_2PbSnBr_6$, b) J-V curve, c) quantum efficiency for heterojunction.

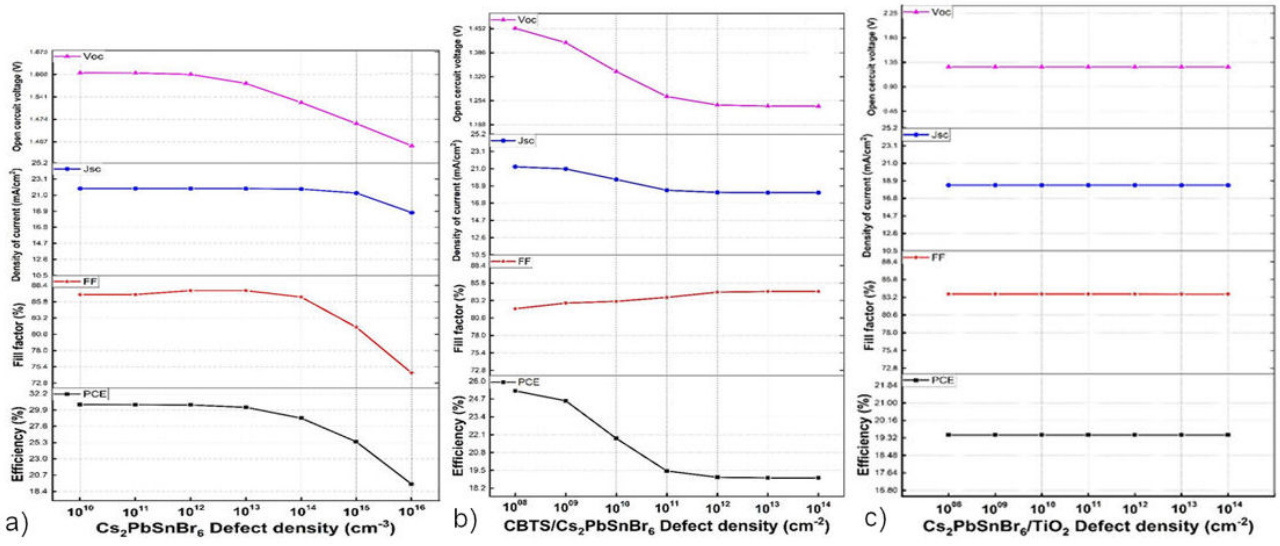


FIGURE 8. Impact of defect density: a) perovskite bulk, b) interface HTL/Absorber, c) interface Absorber/ETL.

mance at low absorber defect densities, with $V_{oc}$, $J_{sc}$, FF, and PCE remaining almost constant up to approximately $10^{13}$ cm$^{-3}$. In this range, minimal recombination ensures efficient carrier collection and a power conversion efficiency close to 30%. However, as the defect density surpasses this threshold, trap-assisted recombination becomes significant, causing a pronounced decline in $V_{oc}$ and FF, while $J_{sc}$ exhibits only a slight reduction. This degradation leads to a sharp drop in PCE, reaching around 19% at a defect density of $10^{16}$ cm$^{-3}$. These results highlight that $Cs_2PbSnBr_6$

demonstrates good defect tolerance at moderate concentrations, being able to withstand defect densities up to $10^{15}$ $cm^{-3}$ while still maintaining good efficiency.

Figure 8b) shows the impact of CBTS/$Cs_2PbSnBr_6$ interface defect density, where we notice that there is sensitivity of the device performance to interface quality. At low defect densities ($10^8 - 10^9$ $cm^{-2}$), the device maintains high $V_{oc}$ (1.4 V), $J_{sc}$ (21 mA/$cm^2$), and efficiency (24%), with only slight variations in FF (83%). As the defect density increases beyond $10^{10}$ $cm^{-2}$, $V_{oc}$ begins to decline due to enhanced interface recombination, while $J_{sc}$ also decreases gradually as carrier collection is impeded. Interestingly, FF remains relatively stable or slightly improves, suggesting that the primary impact of interface defects is on recombination rather than resistive losses. The PCE shows a significant drop from 25% at $10^8$ $cm^{-2}$ to 19% at $10^{14}$ $cm^{-2}$, driven mainly by the reduction in $V_{oc}$ and $J_{sc}$. The reason is that double perovskite devices with tin (Sn) substitution show a significant drop in power conversion efficiency (PCE) on the order of 30 - 40% when the defect density at the interface exceeds about $10^{12}$ to $10^{13}$ $cm^{-2}$ [45].

Figure 8c) illustrates the impact of the $Cs_2PbSnBr_6$/ETL interface, showing that the photovoltaic parameters remain nearly constant over defect densities ranging from $10^8$ to $10^{14}$ $cm^{-2}$. The invariance of these parameters indicates high defect tolerance at the $Cs_2PbSnBr_6/TiO_2$ interface. This stability can be attributed to favorable band alignment, efficient charge separation, and robust electron extraction by $TiO_2$, which collectively suppress recombination losses at moder-

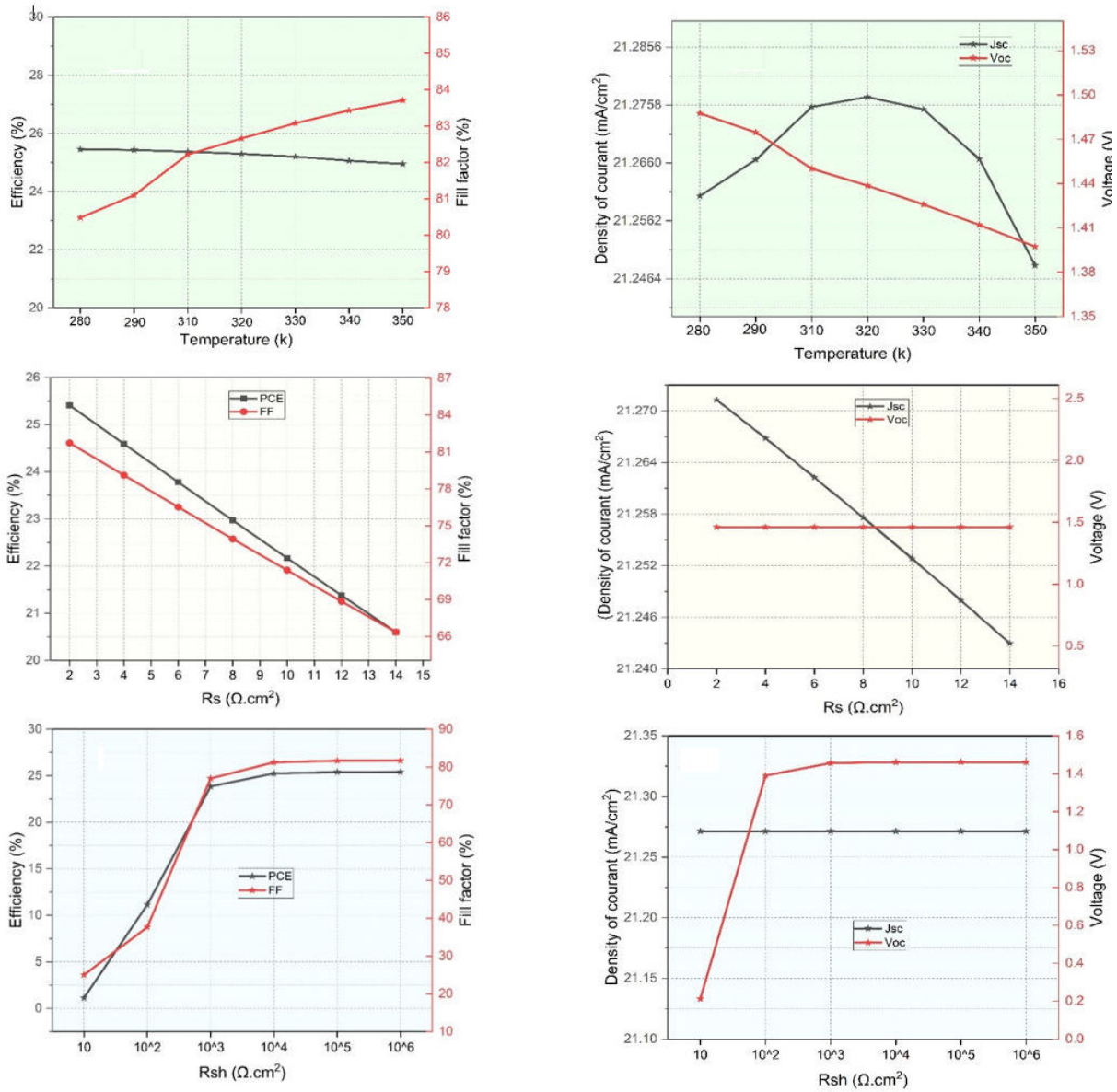


FIGURE 9. Impact of $T$ temperature, $S$ series resistances, and $H$ shunt resistances for HTL/$Cs_2PbSnBr_6$/ETL/FTO.

ate defect levels. These findings are consistent with previous studies on double perovskites and ETL materials, where the quality of the absorber bulk and the $TiO_2$ interface has been identified as key factors in performance optimization [46,47].

### *3.2.3. Impact of temperature, series and shunt resistances in PSC*

The plots in Fig. 9a), 9b) show the variation of PCE, FF, $J_{sc}$, and $V_{oc}$ with temperature (280-350 K). PCE remains highly stable, decreasing only slightly from 25.5% at 280 K to 25.0% at 350 K. FF increases from 79% to 83.5%, likely due to reduced series resistance and enhanced charge mobility at elevated temperatures. $J_{sc}$ rises slightly from 280 K to 320 K before decreasing at higher temperatures, a trend attributed to improved carrier mobility and modest bandgap narrowing [48]. $V_{oc}$ decreases steadily from 1.51 V to 1.39 V with increasing temperature, consistent with thermally induced bandgap shifts. Overall, the cell demonstrates exceptional thermal stability, reflecting low defect density, favorable band alignment, and efficient carrier transport, corroborating the conclusions drawn from Fig. 5 regarding the material's strong temperature resilience.

Figure 9c), d) illustrates the impact of series resistance $R_s$ on device performance. As $R_s$ increases from 2 to 14 $\Omega\cdot$ cm$^2$, PCE declines from 25.4% to 20.8%, primarily due to a reduction in FF from 82% to 66%. $J_{sc}$ decreases only marginally (21.27 $\rightarrow$ 21.24 mA/cm$^2$), while $V_{oc}$ remains nearly constant ($\sim$ 1.5 V). The performance loss is primarily due to increased resistive and recombination losses at higher $R_s$ values. Elevated $R_s$ may result from poor electrical contact at the CBTS/$Cs_2PbSnBr_6$ interface, exacerbated by high defect densities at the interface.

Impact of shunt resistance $R_{sh}$ on the performance of the FTO/$TiO_2$/$Cs_2PbSnBr_6$/CBTS heterojunction in Fig. 9e) and 9f). At very low $R_{sh}$ ($\sim$ 10 $\Omega\cdot$cm$^2$), PCE is extremely low ($\sim$ 2%), and FF is 25%. As $R_{sh}$ increases to $10^3 - 10^4$ $\Omega\cdot$cm$^2$, both PCE and FF increase sharply and then saturate at high values (PCE $\approx 25.4\%$, FF $\approx 82\%$). $V_{oc}$ is extremely low (0.2 V) at very low $R_{sh}$, then increases sharply to 1.48 V at $10^3$ $\Omega\cdot$cm$^2$ and stabilizes. $J_{sc}$ remains almost constant (21.28 mA/cm$^2$) across all $R_{sh}$ values. $V_{oc}$ is highly sensitive to $R_{sh}$ because low $R_{sh}$ introduces leakage currents that prevent voltage build-up. $J_{sc}$ is relatively unaffected by $R_{sh}$, since photocurrent generation is not directly influenced by shunt resistance, but PCE output is degraded at low $R_{sh}$ due to poor $V_{oc}$ and FF [49].

## 4. Conclusion

This work presents a comprehensive study of the novel double perovskite $Cs_2PbSnBr_6$, carried out through a combination of density functional theory (DFT) calculations and SCAPS-1D simulations. The results highlight the exceptional potential of $Cs_2PbSnBr_6$ as a high-performance material for photovoltaic applications compared to other perovskites. Structural analysis confirmed its cubic Fm-3m symmetry with excellent mechanical stability, as validated by elastic constants and the Born stability criteria. The elastic modulus (18.88 GPa) and other derived elastic parameters indicate good resistance to deformation, making it suitable for device integration. The electronic structure, calculated using TB-mBJ + SOC, revealed a direct bandgap of 1.63 eV, ideal for light absorption and harvesting. The calculated optical properties confirmed strong light absorption, particularly for photons in the visible spectrum and high-energy photons, along with low reflectivity and suitable dielectric behavior. The thermoelectric properties indicated good thermal stability, strong performance at elevated temperatures, and favorable carrier transport characteristics. SCAPS-1D simulations confirmed outstanding solar cell performance, with a power conversion efficiency (PCE) reaching 31.8% under optimized conditions (absorber thickness of 0.7 $\mu$m). Key parameters included a high open-circuit voltage ($V_{oc} = 1.61$ V), short-circuit current density ($J_{sc} \sim 22.6$ mA/cm$^2$), and fill factor (FF = 86.7%). The quantum efficiency (QE) approached 100% across the visible spectrum, demonstrating excellent charge carrier generation and collection efficiency. The dual functionality of the material in both photovoltaic and thermoelectric devices opens promising avenues for hybrid energy harvesting systems.

## Acknowledgement

We are grateful to the University of RELIZANE for supporting this work, which is included in the project of PRFU NÂ° B00L02UN480120220002. Furthermore, the first author gratefully acknowledges Prof. Marc Burgelman, University of Ghent, Belgium for providing the SCAPS-1D version 3.3.11 simulation software. And Northwestern University for the program Wien2k.

**Declaration of interest statement**

The authors declare no competing financial interest and any conflict of interest by the reader. If there are other authors, they declare that they have no known competing financial interests or personal relationships that could have appeared to influence the work reported in this paper.

1. M. Ghaleb, A. Arrar, and Z. Touaa, Optimization and Performance Analysis of a TiO2/i-CH3NH3SnBr3/CsPbI3/Al(BSF) Heterojunction Perovskite Solar Cell for Enhanced Efficiency, *ACS Omega* **8** (2023) 37011, https://doi.org/10.1021/ACSOMEGA.3C03891.
2. A. Kojima, K. Teshima, Y. Shirai, and T. Miyasaka, Organometal halide perovskites as visible-light sensitizers for photovoltaic cells, *J. Am. Chem. Soc.* **131** (2009) 6050.
3. C. Lin, Stabilizing Organic-Inorganic Lead Halide Perovskite Solar Cells With Efficiency Beyond 20%, *Front. Chem.* **8** (2020) 556931, https://doi.org/10.3389/FCHEM.2020.00592.
4. S. Brittman, G. W. P. Adhyaksa, and E. C. Garnett, The expanding world of hybrid perovskites: Materials properties and emerging applications, *MRS Commun.* **5** (2015) 7, https://doi.org/10.1557/MRC.2015.6.
5. M. Ghaleb, A. Arrar, A. Hadji Chikh, H. Bendjilali, and O. Zerrouki, I-MASnBr3/CZTGS Heterojunction Solar Cell Layer Optimization Investigated Using Scaps-1D Software Exhibited Excellent Performance at 50 %, *Ann. West Univ. Timisoara - Phys.* 0 (2024) , https://doi.org/10.2478/AWUTP-2024-0012.
6. S. Sandhu and N.-G. Park, Methodologies to Improve the Stability of High-Efficiency Perovskite Solar Cells, *Acc. Mater. Res.* **5** (2024) 1544, https://doi.org/10.1021/accountsmr.4c00237.
7. J. Li *et al*., Biomass-derived functional additive for highly efficient and stable lead halide perovskite solar cells with built-in lead immobilisation, *Energy Environ. Sci.* **18** (2025) 5632, https://doi.org/10.1039/D4EE06038E.
8. T. A. Chowdhury *et al*., Stability of perovskite solar cells: issues and prospects, *RSC Adv.* **13** (2023) 1787, https://doi.org/10.1039/D2RA05903G.
9. M. Ghaleb, A. Arrar, C. A. Hadji, H. Bendjilali, and O. Zerrouki, The Structural, Electronic, Elastic, and Optical Properties of New Double Perovskite Cs2CdPbI6 were Investigated Using a DFT and SCAPS-1D Simulation, *J. Inorg. Organomet. Polym. Mater.* (2025) , https://doi.org/10.1007/s10904-024-03545-y.
10. S. Yeong Hong *et al*., Recent progress in Pb-, Sn-, and Pb-Sn-based inorganic perovskite solar cells: toward enhanced stability and efficiency, *EES Sol.* **1** (2025) 441, https://doi.org/10.1039/D5EL00065C.
11. D. Im, W. C. Choi, G. S. Han, and S. Lee, Recent Advances in Modulating the Crystallization Dynamics of Sn-Pb Mixed Perovskites for High-Efficiency All-Perovskite Tandem Solar Cells, *ChemSusChem* **18** (2025) e202501511, https://doi.org/10.1002/CSSC.202501511.
12. Y. Bai *et al*., Lattice stabilization and strain homogenization in Sn-Pb bottom subcells enable stable all-perovskite tandems solar cells, *Nat. Commun.* **16** (2025) 7344, https://doi.org/10.1038/s41467-025-62661-6.
13. I. Ahmed, K. Prakash, and S. M. Mobin, Lead-free perovskites for solar cell applications: recent progress, ongoing challenges, and strategic approaches, *Chem. Commun.* **61** (2025) 6691, https://doi.org/10.1039/D4CC06835A.
14. S. K. Biswas *et al*., A Numerical Approach to Analysis of an Environment-Friendly Sn-Based Perovskite Solar Cell with SnO2 Buffer Layer Using SCAPS-1D, *Adv. Mater. Sci. Eng.* **2023** (2023) 4154962, https://doi.org/10.1155/2023/4154962.
15. G. A. Nowsherwan, Performance engineering of Cs2InSbCl6 lead-free double perovskite solar cells: insights from DFT, SCAPS-1D, wxAMPS, AFORS-HET, Oghmanano, and COMSOL, *Discov. Mater.* (2025) , https://doi.org/10.1007/S43939-025-00466-6.
16. H. Laltlanmawii *et al*., Cu2XSiS4 (X = Ge, Sn, and Pb) materials for solar-cell applications: A DFT+SCAPS-1D simulation, arXiv:2509.20845 (2025) , https://arxiv.org/pdf/2509.20845.
17. W. Kohn and L. J. Sham, Self-consistent equations including exchange and correlation effects, *Phys. Rev.* **140** (1965) A1133, https://doi.org/10.1103/PhysRev.140.A1133.
18. P. Blaha, K. Schwarz, G. K. Madsen, D. Kvasnicka, and J. Luitz, WIEN2K, in An augmented plane wave + local orbitals program for calculating crystal properties, edited by K. Schwarz (University of Technology, Austria, 2001).
19. Accuracy of generalized gradient approximation functionals for density functional perturbation theory calculations, arXiv:1309.4805 (n.d.) , https://arxiv.org/abs/1309.4805.
20. J. H. Yang, D. A. Kitchaev, and G. Ceder, Rationalizing accurate structure prediction in the meta-GGA SCAN functional, *Phys. Rev. B* **100** (2019) 035132, https://doi.org/10.1103/PhysRevB.100.035132.
21. S. Arora, D. S. Ahlawat, and D. Singh, DFT estimation of structural parameters and band gaps of III-V (GaP, AlP, InP, BP) and II-VI (BeX, MgX, CdX: X = O, S, Se, Te) semiconductors, *Pramana* **97** (2023) 108, https://doi.org/10.1007/s12043-023-02577-2.
22. M. Laurien and O. Rubel, Benchmarking exchange-correlation potentials with the mstar60 dataset: Importance of the nonlocal exchange potential for effective mass calculations in semiconductors, *Phys. Rev. B* **106** (2022) 045204, https://doi.org/10.1103/PhysRevB.106.045204.
23. M. Burgelman, P. Nollet, and S. Degrave, Modelling polycrystalline semiconductor solar cells, *Thin Solid Films* **361** (2000) 527, https://doi.org/10.1016/S0040-6090(99)00825-1.
24. F. Birch, Finite Elastic Strain of Cubic Crystals, *Phys. Rev.* **71** (1947) 809, https://doi.org/10.1103/PhysRev.71.809.
25. N. A. Noor *et al*., Analysis of direct band gap A2ScInI6 (A=Rb, Cs) double perovskite halides using DFT approach for renewable energy devices, *J. Mater. Res. Technol.* **13** (2021) 2491, https://doi.org/10.1016/J.JMRT.2021.05.080.
26. C. A. Hadji, A. Arrar, M. Ghaleb, O. Zerrouki, and H. Bendjilali, Structural, elastic, optoelectronic, thermodynamic and thermoelectric properties of the new halide double perovskite Cs2CaGeI6: first-principles study, *Eur. Phys. J. B* **98** (2025) 100, https://doi.org/10.1140/EPJB/S10051-025-00949-8.

27. C. Ali Hadji, A. Arrar, M. Ghaleb, H. Bendjilali, and O. Zerrouki, Ab initio study of the optoelectronic and thermoelectric properties of the new double perovskite Cs2ZnPbX6 (X=Br, Cl), *Mater. Sci. Eng. B* **310** (2024) 117707, https://doi.org/10.1016/J.MSEB.2024.
28. K. Kim and F. Milstein, Relation between hardness and compressive strength of polymer concrete, *Constr. Build. Mater*. **1** (1987) 209, https://doi.org/10.1016/0950-0618(87)90033-X.
29. J. Kim, L. T. Duy, B. Ahn, and H. Seo, Pre-oxidation effects on properties of bismuth telluride thermoelectric composites compacted by spark plasma sintering, *J. Asian Ceram. Soc.* **8** (2020) 211, https://doi.org/10.1080/21870764.2020.1723197.
30. P. Y. Yu and M. Cardona, Electronic Band Structures, in Fundamentals of Semiconductors, Graduate Texts in Physics (Springer, Berlin, Heidelberg, 2010), https://doi.org/10.1007/978-3-642-00710-1_2.
31. C. Kittel and P. McEuen, Introduction to Solid State Physics (Wiley, 2018).
32. D. R. Penn, *Phys. Rev.* **128** (1962) 2093.
33. F. Mouhat and F.-X. Coudert, Necessary and Sufficient Elastic Stability Conditions in Various Crystal Systems, *Phys. Rev. B* **90** (2014) 224104.
34. M. Jamal, J. S. Asadabadi, I. Ahmad, and A. H. A. Rahnamaye, Elastic constants of cubic crystals, *Comput. Mater. Sci*. **95** (2014) 592.
35. J. Liu, T. Ohkubo, S. Mitani, K. Hono, and M. Hayashi, Correlation between the spin Hall angle and the structural phases of early 5d transition metals, *Appl. Phys. Lett*. **107** (2015) 232408, https://doi.org/10.1063/1.4937452.
36. G. K. H. Madsen and D. J. Singh, BoltzTraP. A code for calculating band-structure dependent quantities, *Comput. Phys. Commun.* **175** (2006) 67.
37. G. K. H. Madsen, BoltzTraP2 (Institute of Materials Chemistry, TU Wien, Austria, 2020).
38. T. Pandey, F. M. Peeters, and M. v. Milošević, High thermoelectric figure of merit in p-type Mg3Si2Te6: role of multi-valley bands and high anharmonicity, *J. Mater. Chem. C* **11** (2023) 11185, https://doi.org/10.1039/D3TC02169F.
39. R. Kikuchi and A. Yamakage, Band curvature effects on quantum transport of spin-1 chiral fermion systems, *Phys. Rev. B* **111** (2025) 125201, https://doi.org/10.1103/PhysRevB.111.125201.
40. T. Heilpern *et al*., Determination of hot carrier energy distributions from inversion of ultrafast pump-probe reflectivity measurements, *Nat. Commun.* **9** (2018) 1853, https://doi.org/10.1038/s41467-018-04289-3.
41. M. K. Hossain *et al*., Numerical simulation and optimization of a CsPbI3-based perovskite solar cell to enhance the power conversion efficiency, *New J. Chem.* **47** (2023) 4801, https://doi.org/10.1039/D2NJ06206B.
42. L. T. B. Pham *et al*., Design of Thermodynamically Stable Lead-Free Cs2InCuCl6 Double Perovskite Solar Cells, *Adv. Theory Simul.* (2025) , https://doi.org/10.1002/adts.202500258.
43. N. Chawki, M. Rouchdi, and B. Fares, Numerical study of BaZrS3 based chalcogenide perovskite solar cell using SCAPS-1D device simulation, **1** (2022) 1251663, https://doi.org/10.21203/rs.3.rs-1251663/v1.
44. K. Fatema and M. Shawon, Analysis of Performance Parameters and Efficiency Enhancement of Double Halide Inorganic Ti-Based (Cs2TiI6) Perovskite Solar Cell Using SCAPS-1D, *Mater. Res. Express* (2025) , https://doi.org/10.1088/2053-1591/AE28C0.
45. M. A. Uddin, S. Rahman, and T. Zaman, Design and simulation of Cs2SnI6 based perovskite solar cell, *Next Mater.* **9** (2025) 100980, https://doi.org/10.1016/J.NXMATE.2025.100980.
46. D. Prochowicz *et al*., Suppressing recombination in perovskite solar cells via surface engineering of TiO2 ETL, *Sol. Energy* **197** (2020) 50, https://doi.org/10.1016/J.SOLENER.2019.12.070.
47. D. K. Sarkar *et al*., Lead free efficient perovskite solar cell device Optimization and defect study using Mg doped CuCrO2 as HTL and WO3 as ETL, Sol. Energy **243** (2022) 215, https://doi.org/10.1016/j.solener.2022.07.013.
48. P. Singh and N. M. Ravindra, Temperature dependence of solar cell performance an analysis, *Sol. Energy Mater. Sol. Cells* **101** (2012) 36, https://doi.org/10.1016/J.SOLMAT.2012.02.019.
49. Y. Li *et al*., Characteristics and sources of volatile organic compounds (VOCs) in Xinxiang, China, during the 2021 summer ozone pollution control, *Sci. Total Environ*. **842** (2022) 156746, https://doi.org/10.1016/J.SCITOTENV.2022.156746.
50. M. Tarekuzzaman, M. H. Ishraq, A. S. Sarker, M. Z. Hasan, and S. S. Hasan, Next-generation solar absorber candidate Rb2PdTe2: a study based on DFT, SCAPS-1D, and machine learning approaches, *J. Mater. Sci*. (2025) 1, https://doi.org/10.1007/S10853-025-11969-1.
51. A. Mohandes and M. Moradi, Achieving 27.20% efficiency for a lead-free double perovskite solar cell with all inorganic Cs2BiAgI6 using AZO UTL as a passivation layer, *Mater. Adv.* **6** (2025) 1520, https://doi.org/10.1039/D4MA01280A.
52. A. Aggarwal, M. Raj, A. Narayan, A. Kushwaha, and N. Goel, Machine learning-guided design of Cs2SnBr6-based solar cells: a DFT and SCAPS-1D analysis with N-doped TiO2 HTL, *Phys. Scr.* **100** (2025) 085946, https://doi.org/10.1088/1402-4896/ADF3FC.